Phase diagram of an empirical potential: The case of Fe-Cu

E. M. Lopasso,[1] M. Caro,[1] A. Caro,[2] and P. E. A. Turchi[2]
[1]*Centro Atómico Bariloche, 8400 Bariloche, Argentina*
[2]*Lawrence Livermore National Laboratory. P.O. Box 808 L-371, Livermore, California 94551, USA*
(Received 31 July 2003; revised manuscript received 30 September 2003; published 24 December 2003)

Molecular dynamics simulations are used to calculate the Gibbs free energy in the entire compositional range of Fe-Cu alloys described with a set of embedded atom potentials available in the literature. Thermodynamic integration and switching Hamiltonian techniques are used to obtain the phase diagram at high temperatures (neglecting phonon quantum effects and electronic contributions) with no further approximations. Limitations of the model were confirmed, such as the absence of the γ and δ phases, a bcc to fcc transformation before melting for pure Fe, the unexpected existence of a stable bcc phase in pure Cu at high T, and consequently complete solid solubility of Fe in Cu in the bcc phase in some temperature range. This work seeds light on the power and limitations of the empirical description of complex systems.

DOI: 10.1103/PhysRevB.68.214205 PACS number(s): 81.30.Bx, 82.60.Lf, 02.70.Ns

INTRODUCTION

Steels in nuclear reactor pressure vessels undergo embrittlement as a consequence of radiation damage. Copper, an impurity present in commercial steels in a saturated solid-solution phase, precipitates as a consequence of the microstructure damage generated by energetic neutrons. These precipitates, which act as obstacles for dislocation motion, are one of the most significant contributions to embrittlement. Therefore, understanding the precipitation process and the evolution of the precipitate structure is an important step in the description of the embrittlement process.

The experimental contributions to the study of this phenomenon started long ago, and more complexity was continuously added to the picture. In 1960, Hornbogen showed that, on aging, precipitation of Cu from α-Fe occurs first by the formation of spherical Cu clusters that transforms into fcc Cu when they become large enough.[1] In 1965, Speich and Oriani demonstrated that these spherical Cu particles subsequently transform into rods upon further aging.[2] In 1990, Pizzini *et al.* reported a direct observation of small clusters having a bcc structure in the peak hardness condition,[3] and Buswell *et al.* reported the development of a distribution of precipitate sizes with aging time.[4] Aging causes the precipitates to grow past a critical size where they undergo a phase transformation from bcc to a close-packed structure.

Phythian *et al.* assumed that this close-packed structure is fcc.[5] However, in 1994 Othen *et al.* concluded that the intermediate-sized (7–15 nm) Cu precipitates have a twinned 9R structure, probably transform martensitically into 9R, and grow in this structure from a diameter of 6 nm up to at least 15 nm.[6] Shortly after Othen *et al.* concluded that, during aging at 550 °C, the bcc-to-9R martensitic transformation of Cu precipitates occurred at a size of about 4 nm,[7] with complementary studies on the role of temperature. Recently in 2000, Monzen *et al.* reported more high-resolution electron microscope (HREM) images of twinned 9R Cu precipitates in a Fe-Cu alloy aged at 550 °C.[8]

The three-dimensional (3D) atom probe technique has recently shown that precipitates in ferritic steels have a complex chemical composition that includes Cu, Mn, Ni, Si, and P.[9]

The complexity of the processes fueled a significant effort from the computational materials science community. At present, a contribution to the microscopic knowledge about these phenomena comes from both *ab initio* calculations[10–12] and classic molecular dynamics (MD) and Monte Carlo (MC) simulations, mostly based on the embedded atom model for the atomic interactions.[13] In what follows we focus on classic potentials and in particular in the way they have been used to study properties of the Fe-Cu system. In this paper we are interested in the capabilities and limitations of the model potential to describe the thermodynamics of the alloy.

In 1990 Phythian *et al.*[14,15] reported a MD simulation that supported the first direct experimental evidence that the small Cu precipitates (2 nm) have bcc structure. They used interatomic potentials for pure Cu derived in 1987 by Ackland *et al.*[16] The simulations predict for bulk Cu a metastable bcc structure with lattice parameter larger than that of α-Fe. However, in both of these papers Cu precipitates in an α-Fe matrix could not be simulated because of the absence of a Fe-Cu potential. In 1995, Osetsky *et al.* published a series of papers on the Fe-Cu system. In Ref. 17 they present potentials for the pure elements; in Ref. 18 they report the first pair potentials for Fe-Cu system, used to simulate small Cu clusters and coherent precipitates in the bcc-Fe matrix. In Ref. 19, MD is used to examine vacancy migration inside Cu precipitates in Fe. A key result was that precipitates act as vacancy traps, implying that during growth the precipitates can absorb vacancies.

In 1997 Odette *et al.* reported lattice-MC (LMC) simulations for complex Cu-Mn-Ni-Si structures in Fe.[20] LMC cascade aging simulations were done using pair potentials based on a regular solution theory (RST) approximation. They report parameters of the lattice embedded-atom-model (EAM) Fe-Cu potential used in LMC cascade aging simulations. In 1999, Wirth *et al.* on one side[21] and Domain *et al.* on the other[22] performed kinetic-LMC simulations of Fe-Cu alloys. These authors focused specifically on the development of vacancies and Cu clusters after irradiation damage. These

simulations confirm the presence of high vacancy concentrations in the precipitates. The results were in good agreement with small-angle neutron scattering data.

In 1998, Ludwig *et al.* used static relaxation and a Fe-Cu EAM potential to study the instability of bcc copper precipitates embedded in an α-Fe matrix.[23] In 2001, Le Bouar extended the study of the coherency loss during the bcc-9R transformation of the precipitates also using static simulations and the same Fe-Cu potential developed by Ludwig *et al.*[24]

In 2001, Blackstock and Ackland, reported computer simulations of the phase transition of Cu precipitates in Fe-Cu alloys.[25] For the first time in a simulation a precipitate is followed during the phase transition from the bcc structure coherent with the iron matrix to the twinned 9R crystal structure. They used the interatomic potentials derived in 1997 by Ackland *et al.*[16]

As this brief Introduction shows, the real problem of microstructure evolution of ferritic steels under irradiation involves complex thermodynamics of nonequilibrium and kinetic processes in alloys, while the computational approach is still in its infancy, dealing with an oversimplified description of Fe and Fe-Cu alloys. In fact, the classic many-body potentials, based on the EAM, have extensively been used to get insight into complex processes in several types of simple solids, in particular transition metals and some of their alloys.[26–27] Extensive work has been done in the application of this model to many solid solutions and intermetallic compounds, but limited effort was devoted to the calculation of the complete equilibrium phase diagram predicted by this type of approximation and, from there, of the driving forces that govern nonequilibrium processes. In summary, little is still known about the ability of empirical n-body potentials to reproduce details of equilibrium phase diagrams of transition-metal alloys.

In this work, we consider one of the EAM potentials for Fe-Cu developed by Ackland *et al.*[16] to extract the phase diagram of this model alloy. We report Gibbs free energies calculated using MD simulations for pure elements and alloys in both the fcc and bcc solid phases, and for the liquid phase. We follow the procedure that we already applied to the study of the Au-Ni system.[28] To our knowledge this is the first calculation of a noncoherent phase diagram from the knowledge of an empirical EAM potential. No approximations are used in the formalism to calculate the phase diagram besides those coming from a classic potential: no quantum phonon effects and no electronic or magnetic degrees of freedom. However, the numerical evaluations, on their side, have uncertainties originated in both the finite size of the samples and the finite time used in the averages, which determine the overall accuracy of the results.

FREE-ENERGY CALCULATION

For details on the calculation of the free energy, we refer the reader to our previous publication.[28] Here we highlight the basic aspects of the method, as well the differences with this multiphase case. For convenience, in the derivation that follows we shall not make a distinction between Gibbs, g, and Helmholtz, f, free energies, as well as internal energy and enthalpy, because some integrals or averages can be better calculated at constant V and others at constant P. For clarity however, steps are formulated in terms of f or g to make the ensemble where the calculation is done explicit.

We calculate the free energy per particle at a given temperature T, $f(T)$, through a thermodynamic integration between the state of interest and a reference state at temperature T_0 with known free energy $f(T_0)$, using the Gibbs-Duhem equation

$$f(T)=f(T_0)\frac{T}{T_0}-T\int_{T_0}^{T}\frac{h(\tau)}{\tau^2}d\tau, \tag{1}$$

where $h(\tau)$ is the enthalpy per particle. The enthalpy is obtained from a MD run and it is fitted with a second-order polynomial in T, which allows an analytic integration in Eq. (1).

The coupling-constant integration method, or switching Hamiltonian method,[29] is used to calculate $f(T_0)$. We consider a system with Hamiltonian $H=(1-\lambda)W+\lambda U$, where U describes the actual system (in this work, described with a EAM-type Hamiltonian) and W is the Hamiltonian of the reference system, with known free energy. The parameter λ allows us to switch from U (for $\lambda=1$) to W (for $\lambda=0$). With this Hamiltonian we can obtain the free-energy difference between W and U by calculating the reversible work required to switch from one system to the other. Then the unknown free energy associated with U, $f(T_0)$, is given by

$$f^{Sol}(T_0)=f_W(T_0)+\Delta f_1,$$

$$\Delta f_1=\frac{1}{N}\int_0^1\left\langle\frac{\partial H}{\partial\lambda}\right\rangle d\lambda=\frac{1}{N}\int_0^1\langle U-W\rangle_\lambda d\lambda, \tag{2}$$

where $f_W(T_0)$ is the free energy of the reference system at T_0. The integration is carried over the coupling parameter λ, which varies between 0 and 1, and $\langle\cdots\rangle$ stands for the average over a canonical ensemble, or a time average in a (T, V, N) constant MD simulation.

For the solid phases the reference system W is a set of Einstein oscillators centered on the average positions of the atoms in the (T_0, $P=0$, N) ensemble corresponding to the Hamiltonian U. The noninteracting Einstein oscillators have no internal pressure, so their ensemble is the (T, V, N) one. The free energy per atom of the Einstein crystal is[30]

$$f_{Eins}=-3k_BT_0\ln(T_0/T_E), \tag{3}$$

where T_E is the Einstein temperature of the oscillators, $T_E=\hbar\omega_E/k_B$ where k_B is the Boltzmann constant, ω_E is the Einstein frequency of oscillations, and $\hbar$ is the Planck constant divided by 2π.

For the liquid phase, the reference system W is an ideal gas at the same temperature and density as the EAM sample. The process to switch from U to W involves an intermediate step to avoid particle overlap during the integration. First, we compute the free-energy difference between the true system with potential U (the EAM potential)and a system with a repulsive potential W_L (soft spheres). In this work, we use

$W_L = 0.1U^{rep}$, where U^{rep} is the pair potential part of the EAM energy, which is purely repulsive for the potential we are using. As in the solid phase, the integration is carried over the coupling parameter λ, which varies between 0 and 1. The system is kept at the constant volume V_0, which equilibrates the U Hamiltonian at temperature T_0 and $P = 1$ bar. Therefore, the free-energy change for a pure element due to the switch is given by Δf_1, as in the second line of Eq. (2).

The second step is a reversible expansion of the repulsive gas, from V_0 and high pressure, to reach the low-density limit (where it becomes identical to the ideal gas), followed by a reversible compression of the ideal gas, to recover the initial density or volume. The change in free energy due to both processes is

$$\Delta f_2 = k_B T_0 \int_0^{\rho_0} \left[\frac{P}{\rho k_B T_0} - 1 \right] \frac{d\rho}{\rho}, \tag{4}$$

where $\rho_0 = N/V_0$ is the particle density. After the processes represented by Eq. (4) have taken place we end up with an ideal gas at (T_0, ρ_0), whose free energy is given by $f_W^{Liq} = k_B T_0[\ln(\rho_0 \Lambda^3) - 1]$, where Λ is the de Broglie thermal wavelength ($\Lambda^2 = h^2/2\pi m k_B T_0$), with h the Planck constant and m the atomic mass.[30] Then the free energy of the liquid phase is calculated as the sum of these contributions:

$$g^{Liq}(T_0) = \Delta f_1 + \Delta f_2 + f_W^{Liq}(T_0, \rho_0). \tag{5}$$

Equations (1)–(5) give the free energies of the solid and liquid phases for the pure elements as a function of temperature.

ALLOYS

The strategy for the alloy calculations is to construct for each of the three phases $\phi = \{\text{bcc,fcc, and liquid}\}$ a set of free-energy functions versus temperature $g_c^\phi(T)$, for several values of the composition c, extract from them $g_T(c)$ curves, and then perform the common tangent construction to determine the phase diagram.

The equations presented so far are readily applicable to alloys provided the samples used for both the switching and the enthalpy evaluations are large enough to self-average the diversity of short-range configurations that appears in a real macroscopic sample. Similarly, the free energies of the reference mixture of Einstein oscillators can be calculated using the following expression:[29]

$$f_{Eins}(c, T_0) = c \; f_{Eins}^{Cu} + (1-c) f_{Eins}^{Fe} - T_0 s_{conf}(c), \tag{6}$$

where c measures the Cu composition, and f_{Eins}^{Cu} and f_{Eins}^{Fe} are given by Eq. (3). The configurational entropy per particle, $s_{conf}(c)$, is given by the usual expression $-k_B[c\ln(c) + (1-c)\ln(1-c)]$, assuming the solution is completely random. For the ideal gas,

$$f_{id}(c, T_0, \rho) = c \; f_{id}^{Cu}(\rho_{Cu}) + (1-c) f_{id}^{Fe}(\rho_{Fe}) \tag{7}$$

or, making the entropy of mixing appear explicitly,

$$f_{id}(c, T_0, \rho) = c \; f_{id}^{Cu}(\rho) + (1-c) f_{id}^{Fe}(\rho) - T_0 s_{conf}(c), \tag{8}$$

where ρ is the total density, ρ_{Cu} and ρ_{Fe} are the partial densities [$c\rho$ and $(1-c)\rho$, respectively], and the f_{id}^i's are given in the preceding section.

In summary, the steps and equations used in this work are

(i) MC generation of solid-solution samples in both solid phases and

(ii) MD runs to determine the enthalpy vs T for solid solutions for different compositions and phases. For some compositions and phase (fcc or bcc) this step may not be doable if the sample is too far from equilibrium, because spontaneous transformation to the equilibrium phase may occur. Those situations are not relevant for the determination of the equilibrium phase diagram.

(iii) Second-order polynomial fits to the enthalpy:

$$h^\phi(c, T) = a_c^\phi + b_c^\phi T + c_c^\phi T^2. \tag{9}$$

(iv) Analytic integration of the Gibbs-Duhem relations, Eq. (1), using a polynomial expression for h:

$$-T \int_{T_0}^{T} \frac{h^\phi(c, \tau)}{\tau^2} d\tau = a_c^\phi - b_c^\phi T \ln(T) - c_c^\phi T^2 + d_c^\phi T. \tag{10}$$

(v) MD simulations of the switching Hamiltonian process to obtain $\langle U - W \rangle$ for the three phases and at each composition.

(vi) Δf_1 evaluation via analytic integration of sixth-degree polynomial fits to $\langle U - W \rangle$.

(vii) MD simulations of the adiabatic expansion of the repulsive fluid, Eq. (4), at each composition.

(viii) Δf_2 evaluation via analytic integration of sixth-degree polynomial fits to the integrand in Eq. (4).

(ix) Second-order polynomial fits to the coefficients $a^\phi(c)$, $b^\phi(c)$, $c^\phi(c)$, and $d^\phi(c)$, as functions of composition.

These lead to the following general equation for the free energy of each phase ϕ:

$$g^\phi(c, T) = a^\phi(c) - b^\phi(c) T \ln(T) - c^\phi(c) T^2 + d_G^\phi(c) T - T s_{conf}(c). \tag{11}$$

In this last expression, the fourth term comes from both the integration appearing in Eq. (1) and the first term on the right-hand side of that same equation—namely,

$$d_G^\phi(c) = d^\phi(c) + \frac{1}{T_0} g^\phi(c, T_0). \tag{12}$$

The last term in Eq. (11) is the configurational entropy contribution, conveniently left explicit to provide accurate derivatives close to $c = 0$ and $c = 1$.

SIMULATIONS

We consider the EAM potential of Ackland *et al.*[16] for our simulations, using samples of 686 atoms for the bcc phase

and 500 atoms for the fcc phase.

The generation of samples in either bcc or fcc solid-solution phases represents a delicate issue. In our case, the configurations for different values of the Cu composition were obtained by Metropolis MC runs in the transmutation ensemble ($T=1500$ K, $P=0$, N, $\Delta\mu$), where $\Delta\mu$ is the difference in chemical potentials, adjusted to get the desired composition. Sufficiently long runs (longer than 10^4 MC steps/atom) allow the development of any eventual short-range order, while still retaining the metastable solid solutions, if it happens not to be the equilibrium phase. After equilibration, every MC step generates a possible sample with different enthalpy and composition. Selecting among them those with the desired composition, a histogram of the enthalpy shows a Gaussian-like distribution around a mean enthalpy value. Then we select a sample in the central bin of the histogram as the most representative of all possible local arrangements at that composition. The short-range order appears to be below 0.14 at all compositions in both phases which rules out the existence of ordered phases.

A Nosé thermostat provides the temperature control in MD runs, and constant-pressure simulations use the Parrinello-Rahman algorithm.[31] In all simulations the time step was 2 fsec. The first 10^4 time steps are used to equilibrate the sample, and the statistical average of the thermodynamic variables is performed on the next 10^4 steps. Samples in both solid phases are heated up in successive runs between 0 K and 3000 K, and then cooled down to 0 K, with a temperature interval of 50 K. Solid-to-liquid and liquid-to-solid transformations are observed with large hysteresis due to finite-size effects.

The reference free energy of the solids, $g_c^{\phi}(T_0)$, is calculated at $T_0=296$ K using Einstein temperatures equal to experimental Debye temperatures—i.e., $T_E^{Fe}=470$ K and $T_E^{Cu}=343$ K.[32] The Einstein temperature can in fact be chosen to minimize the structure of the switch curve in order to improve the numerical precision.

To calculate the integral involving the switch, we first cool down the samples to 0 K at the volume corresponding to $P=0$ at $T=296$ K and determine the equilibrium positions $\{r_{i0}\}$, of the Einstein crystal. Typically, we calculate the average $\langle U-W_{Sol}\rangle$ at constant temperature and constant volume, for values of λ varying between 0 and 1 with an interval $\Delta\lambda=0.05$. Again, calculations at a given λ are carried out in two successive runs each of 10^4 steps, and averages $\langle U-W_{Sol}\rangle$ are taken on the second set of time steps. We fit a polynomial curve of sixth degree to these points and solve the integral in Eq. (2) analytically.

In the liquid phase, the Helmholtz free-energy change Δf_1 is evaluated at a reference temperature $T_0=3000$ K. The average volume V_{av} of a sample equilibrated at 3000 K is used to generate a cubic sample with volume $V_0=V_{av}(3000\ \mathrm{K})$. This cubic sample is taken as the starting sample for each run for every value of λ. The switching parameter λ varies between 0 and 1, in intervals of 0.05, and before each $\langle U-W_{Liq}\rangle$ average process we equilibrate the sample, as for the solid case. A sixth-degree polynomial is fitted to the points and the integral of Eq. (2) is solved analytically. We then expand the sample keeping the temperature constant and equal to T_0. This is done in consecutive runs reducing the pressure from about 125 kbar to 1 bar. Two more values are added to this data: the origin ($P=0$, $\rho=0$), corresponding to the ideal gas limit, and the average pressure and density obtained for the case $\lambda=0$. Once the evolution of pressure as a function of density is obtained, we proceed to calculate the integrand of Eq. (4), $P/\rho k_B T-1$, and to fit a sixth-degree polynomial to this function. The Helmholtz free-energy change Δf_2 is obtained by analytical integration of this polynomial.

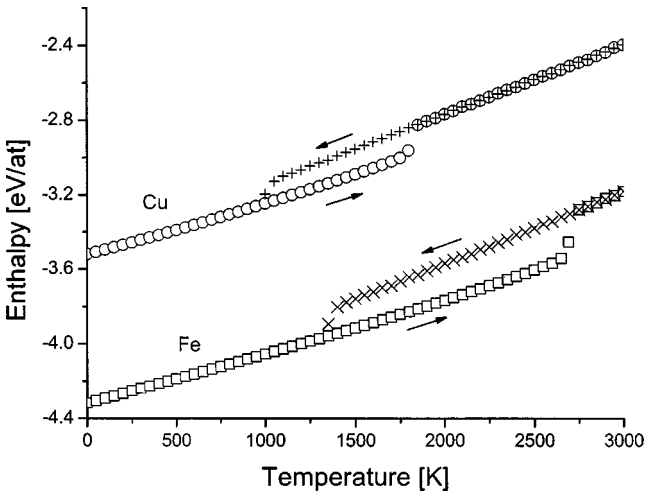

FIG. 1. Enthalpy of Cu and Fe as a function of temperature. Heating and cooling runs are indicated by the arrows.

RESULTS AND DISCUSSION

Figure 1 shows the behavior of the solid and liquid internal enthalpies $h^S_{Fe,Cu}$ and $h^L_{Fe,Cu}$ as a function of temperature. MD runs last 30 psec at each temperature, with an incremental temperature step of 50 K. Discontinuities show the temperature at which solids become liquids and vice versa under the particular conditions of the simulation and do not reflect the thermodynamic melting temperatures. The points shown in the figure correspond to heating and cooling runs, as indicated by the arrows. The latent heat of melting estimated from these figures for pure Fe is 0.221 eV/atoms and for pure Cu 0.134 eV/atoms, while the experimental values are 0.143 eV/atoms and 0.135 eV/atoms, respectively.[33]

Figure 2 shows the integrand in the switching Hamiltonian method, Eq. (2), for both pure elements. Each point is an MD run at constant volume and at $T=296$ K. These curves are essentially featureless, except close to $\lambda=1$, where the negative slope becomes significant. A denser grid of points is used there to ensure a numerical precision of the integral of a few meV/atoms. An important technical point is that in the $\lambda=\sim 0$ region, the dynamics is essentially governed by the noninteracting Einstein oscillators. The thermostat, which provides the energy necessary to keep the isothermal condition, does not provide interaction between the oscillators and, therefore, only the small contribution of the EAM-type Hamiltonian provides the interaction necessary to

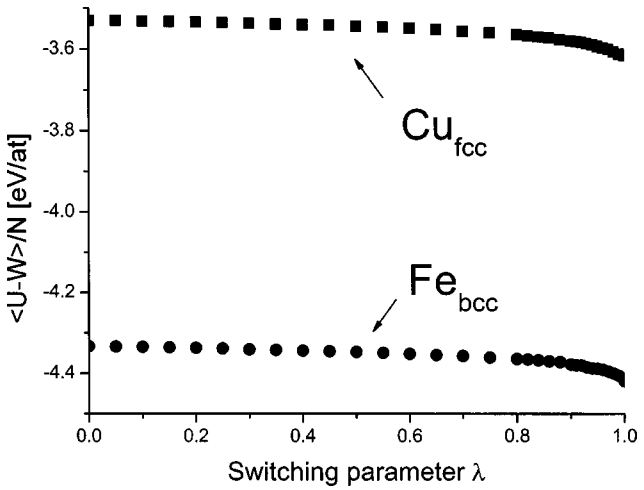

FIG. 2. Average values of $\langle U-W \rangle$ vs λ for bcc Fe and fcc Cu, corresponding to the integrand of the switching Hamiltonian [c.f. Eq. (2)].

reach thermal equilibrium. For this reason, for values of λ close to 0 long runs of up to 100 psec are done as equilibration steps. As mentioned earlier, these curves are fitted with sixth-order polynomials and integrated analytically.

Figure 3 shows the equivalent switching Hamiltonian processes for the liquid phase of both pure elements. Each point is an MD run at constant volume and at $T=3000$ K. In this case the reference potential is the repulsive pair potential. Here again these curves are fitted with a sixth-order polynomial and integrated analytically.

Finally, Fig. 4 shows the last simulation step represented by the adiabatic expansion of the fluid to reach the ideal gas limit at low pressures, where both curves, and in fact for all materials, meet at $P/\rho k_B T=1$. Here again $T=3000$ K. Two open symbols indicate the density corresponding to the pressure arrived at the end of the preceding switching Hamiltonian process, for $\lambda=0$—that is, for the repulsive potential. As is clear, only densities lower or equal to those at $\lambda=0$ are needed, but the simulations run for higher as well as lower densities, corresponding to a range between 1 and 120 kbar,

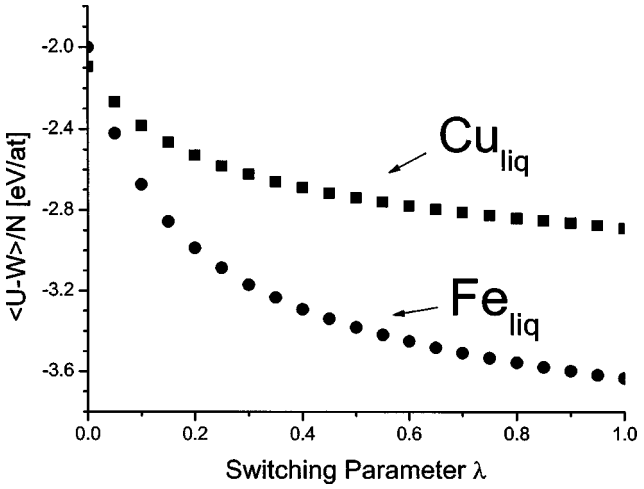

FIG. 3. Same as Fig. 2. for the liquid phases.

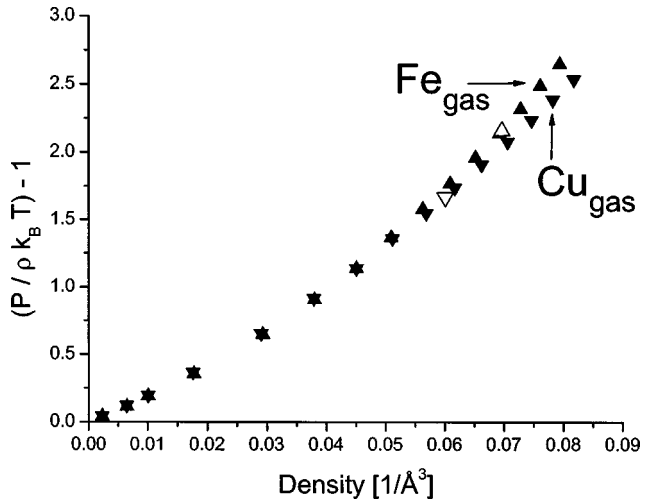

FIG. 4. Evaluation of the integrand of Eq. (4) (expansion and compression cycles) for Fe and Cu in the gas phase. Note the overlap of the curves in the limit of low density (ideal gases).

to gain precision in the sixth-order polynomial used in the fit.

Figures 1–4 show examples of the computational steps to obtain g for the case of pure elements Fe and Cu. It is to be noticed that these steps have to be repeated for every composition from $c=0$ to $c=1$ in the alloy case. In doing so, values of the coefficients a, b, c, and d in Eq. (11) become functions of composition. Tables I(a)–I(c) show these coefficients of the Gibbs free energy g, Eq. (11), for all three phases bcc, fcc, and liquid in terms of their second-degree polynomials in composition c.

For the particular case of $c=0$ or $c=1$, these functions allow us to find the equilibrium phases of the pure elements. Surprisingly, we find that Fe shows a bcc-to-fcc transition just below its melting point, and Cu shows a fcc-to-bcc transition at 0.75 T_m.

For the phase diagram, the usual common tangent construction between the three phases provides the limits of the phase fields. Figure 5 shows as example curves for the excess free energies of the three phases at two temperatures—namely, 1143 K, right at the transition from fcc Cu to bcc Cu and inside the miscibility gap, and at 2000 K where bcc solid solution and liquid coexist. Note the energy scale in these figures and the dispersion of points determined in the numerical simulations, which is of the order of a few meV/atoms. Figure 6 shows the complete phase diagram. An enlarged view of the high-temperature Fe-rich region is shown in Fig. 7.

Comparison between Figs. 6 and 7 and the experimental phase diagram, Fig. 8, redrawn from Ref. 34, shows significant differences. There are three salient features in the calculated diagram—namely, the properties of the pure elements and the properties of the solid solutions. Pure Fe shows a transition to fcc phase right below melting that has no relation to the experimental one, which is driven by magnetism. The melting point of Fe (in the fcc) phase is at 4/3 of the experimental T_m. Here Cu has a transition to a bcc phase at about 3/4 of T_m, which does not appear in real Cu; its

TABLE I. Second-order polynomial fits to the coefficients appearing in Eq. (11) for (a) the bcc phase, (b) the fcc phase, and (c) the liquid phase. Units are such that the resulting free energy is obtained in meV/atoms when the temperature is in K.

Coefficient	Quadratic	Linear	Independent	R^2
		(a)		
a	-2.3340×10^{-01}	$1.0525\times10^{+00}$	$-4.3115\times10^{+00}$	0.99996
b	5.2625×10^{-05}	-1.8929×10^{-05}	2.4080×10^{-04}	0.96928
c	-2.6634×10^{-08}	1.3548×10^{-08}	1.6894×10^{-08}	0.94598
Δf_A	-2.2456×10^{-01}	$1.0501\times10^{+00}$	$-4.3507\times10^{+00}$	0.99996
f_0		-2.4105×10^{-02}	3.5382×10^{-02}	Exact
d_G	3.2143×10^{-04}	-1.9336×10^{-04}	1.3624×10^{-03}	
		(b)		
a	-2.7365×10^{-01}	$1.0182\times10^{+00}$	$-4.2599\times10^{+00}$	0.99973
b	2.4096×10^{-05}	-2.6616×10^{-05}	2.4469×10^{-04}	0.20519
c	1.2173×10^{-08}	8.0491×10^{-09}	8.9973×10^{-09}	0.96553
Δf_1	-2.6284×10^{-01}	$1.0221\times10^{+00}$	$-4.3080\times10^{+00}$	0.99985
f_0		-2.4105×10^{-02}	3.5382×10^{-02}	Exact
d_G	1.7722×10^{-04}	-2.1733×10^{-04}	1.3520×10^{-03}	
		(c)		
a	-1.0897×10^{-01}	9.0441×10^{-01}	$-4.3060\times10^{+00}$	0.99827
b	-8.8953×10^{-05}	1.0958×10^{-04}	3.5475×10^{-04}	0.57650
c	1.2556×10^{-08}	-2.0791×10^{-08}	6.8886×10^{-09}	0.68924
Δf_1	-2.2224×10^{-01}	7.9600×10^{-01}	$-3.2507\times10^{+00}$	0.99994
Δf_2	-1.1117×10^{-01}	4.2365×10^{-02}	4.2398×10^{-01}	0.99779
f_0	2.0187×10^{-02}	-1.0794×10^{-01}	$-3.3942\times10^{+00}$	0.99974
d_G	-7.4261×10^{-04}	7.5694×10^{-04}	2.2226×10^{-03}	

melting point, in the bcc phase, is at 1.14 of the experimental T_m.

The medium temperature region of the alloy shows an eutectoid at $c_{Cu}=0.91$ and a peritectic at $c_{Cu}=0.005$ and a segregating bcc solid solution system with a low mixing energy, producing a miscibility gap that closes in the solid phase, contrary to experiment. As a consequence of this, there is a region around 1600 K of complete solid solubility in the bcc phase.

The behavior of these potentials for the Fe-Cu mixture is modeled on the basis of the dilute limits of the heats of solution. According to Ref. 16, the heat of solution of a single impurity was fitted to unrelaxed values for Cu in Fe and Fe in Cu, both at 0.317 eV. The low-temperature solubility limits at both extremes of the diagram are well above the experimental values. This can be qualitatively understood in terms of the nearby high-temperature phase of Cu (a bcc phase), which makes the concentrated solution much less energetic than the extrapolated dilute limit may suggest.

From these considerations, we conclude that the main effect that affects the entire phase diagram is the existence of a bcc phase of Cu.

As a test of the consistency of these results, we performed MC calculations of the microstructure at two locations in the phase diagram, represented by asterisks in Fig. 6—namely, $Fe_{40}Cu_{60}$ at 1600 K and $Fe_{75}Cu_{25}$ at 900 K, expecting to see a bcc solid solution in the first case and a Cu precipitate in bcc Fe in the second. Figures 9(a) and 9(b) show the resulting configurations, confirming the expectations, with the exception that the Cu precipitate has a coherent bcc structure, probably as a result of a gain in interfacial energy and the fact that bcc Cu is only slightly more energetic than the equilibrium phase which is fcc at this temperature. We point out here again that the bcc precipitate is in agreement with experimental observations and computer simulations, as commented on in the Introduction.

Finally, Figs. 6 and 7 also explain a curious observation from the heating and cooling runs that lead to Fig. 1. Even if we clearly understand that the cooling rate involved in the thermal treatment described earlier in connection to this figure is extremely fast compared to experimental accessible values, our experience indicates that for most potentials under equivalent simulation conditions, samples crystallize in structures without defects. For these potentials, however, the enthalpy of the solid phases on the cooling run lies several meV above the enthalpy on the heating runs, indicating the presence of defects. Visual inspection does not help to elucidate the nature of the defects but the pair correlation function for pure Cu clearly shows traces of bcc structure, confirming the existence of this phase.

We believe the relevance of the present work is twofold. On the one hand, it shows the methodology to construct phase diagrams derived from empirical potentials for a system involving multiple phases. The simpler case of the calculation of a coherent phase diagram for Au-Ni was published earlier.[28] Knowledge of the phase diagram predicted

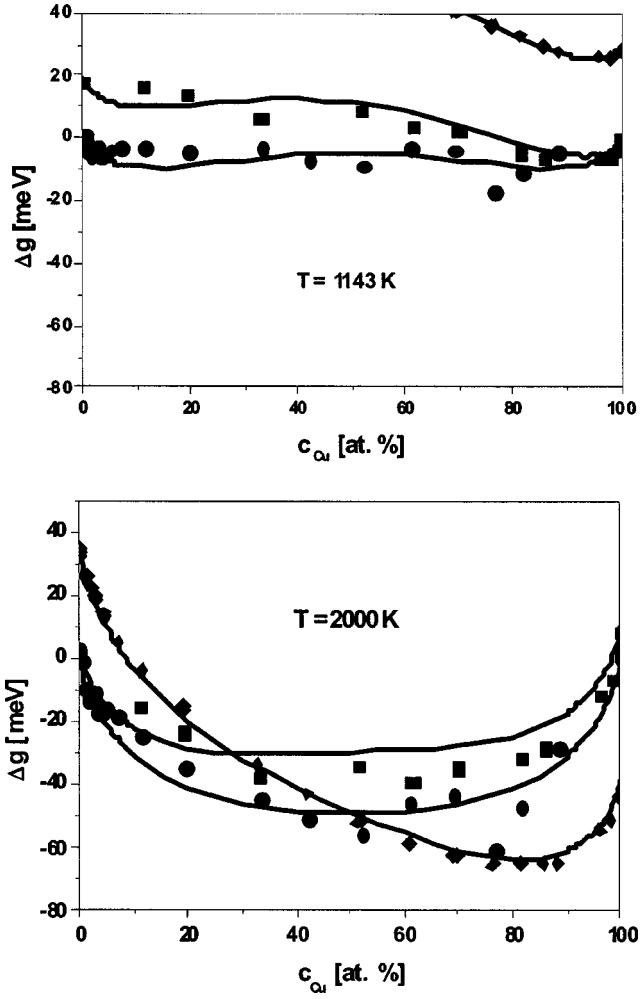

FIG. 5. Example curves for the excess free energies of the three phases at two temperatures, 1142 K, right at the transition from fcc Cu to bcc Cu and inside the miscibility gap, and at 2000 K, where bcc solid solution and the liquid coexist. Rhombuses (liquid), squares (fcc), and circles (fcc).

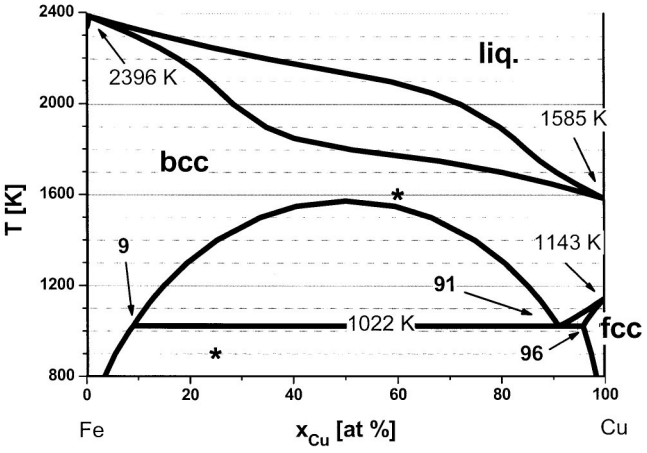

FIG. 6. Phase diagram of Fe-Cu as obtained from the EAM potential of Ref. 16. Note the fcc-to-bcc transition of Cu and the eutectoid at $c_{Cu}=0.91$. Asterisks indicate the composition and temperature of the MC simulations of microstructure reported in Fig. 8.

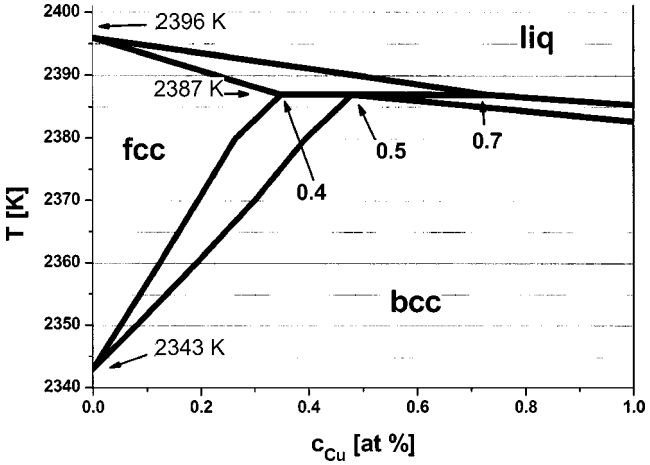

FIG. 7. Enlarged view of Fig. 6 showing the bcc-to-fcc transition of Fe and the peritectic at $c_{Cu}=0.005$.

from empirical potentials is essential for analyzing the results of simulations of equilibrium and nonequilibrium processes. On the other hand, the ability to construct these diagrams can be used in a feedback procedure to improve the empirical potentials themselves. In other terms, is it the enthalpy or the entropy that is responsible for the spurious phases we observe? Is it possible to modify the potentials to avoid these phases without affecting the properties that are correctly predicted? These issues are addressed in a forthcoming paper, where we analyze in detail the enthalpy, entropy, and free energy of the three phases and compare them with standard thermodynamic databases, getting qualitative and quantitative insight into the limitations of the EAM in its present form. In particular, we can highlight the importance of the magnetic contribution to enthalpy and entropy, which is absent in the model.

For the particular case of the Fe-Cu system, another EAM potential by Ludwig *et al.*[23] has extensively been used. Here again, starting from the description of the pure elements given in previously published potentials,[35,36] a cross pair term was designed to reproduce the heat of solution of a single impurity. We are currently studying the phase diagram of such a potential. The results reported in this paper, those

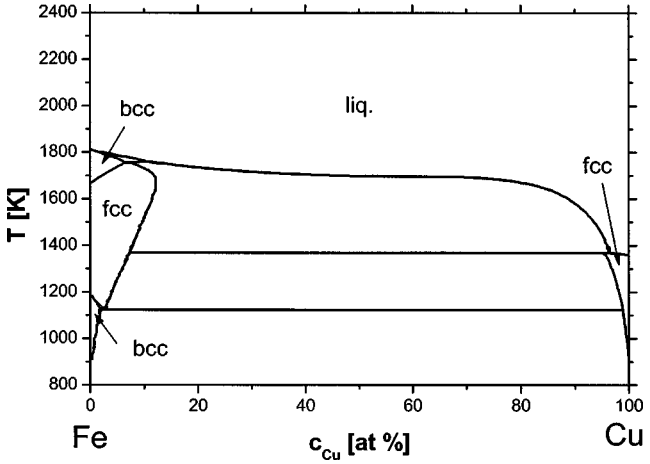

FIG. 8. Phase diagram of Fe-Cu, redrawn from Ref. 34.

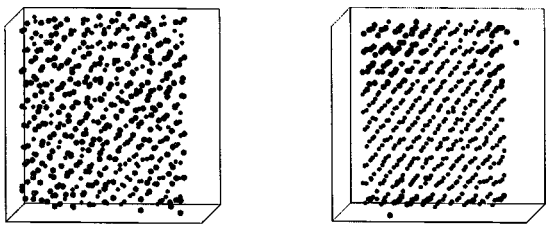

FIG. 9. Monte Carlo calculations of the microstructure at two locations in the phase diagram, $Fe_{40}Cu_{60}$ at 1600 K and $Fe_{75}Cu_{25}$ at 900 K (represented by asterisks in Fig. 6).

for the potential of Ludwig *et al.*, which will come soon, and simulations on microstructure evolution based on a Metropolis or lattice Monte Carlo model based on them, like those of Khrushcheva *et al.*,[37] will provide a deep insight into the model's ability to describe this complex system.

Besides thermodynamic equilibrium phases, microstructure is the consequence of kinetic processes and defect energetics. In particular, shape and phases within the Cu precipitates, such as the bcc-9*R*-fcc transitions mentioned in the Introduction, are determined by interface structures and energies, and size-mismatch-induced stress. These issues are not addressed in equilibrium thermodynamic calculations such as those reported here and would deserve a similar quantitative analysis assessing the adequacy of the model used to describe the right interface energetics.

In summary, these computational thermodynamics procedures can be used to improve the quality of the description of properties of pure metals and alloys, and to better understand the limitations associated with the use of empirical potentials.

ACKNOWLEDGMENTS

This work was performed under the auspices of the U.S. Department of Energy by the University of California, Lawrence Livermore National Laboratory under Contract No. W-7405-Eng-48, and CONICET, Argentina, Grant No. PIP-0664/98.

[1] E. Hornbogen, Trans. Metall. Soc. AIME **218**, 1064 (1960).
[2] G. R. Speich and R. A. Oriani, Trans. Metall. Soc. AIME **233**, 623 (1965).
[3] S. Pizzini, K. J. Roberts, W. J. Phythian, C. A. English, and G. N. Greaves, Philos. Mag. Lett. **61**, 223 (1990).
[4] J. T. Buswell, C. A. English, M. G. Hetherington, W. J. Phythian, G. D. W. Smith, and G. M. Worrall, ASTM Spec. Tech. Publ. **1046**, 127 (1990).
[5] W. J. Phythian, A. J. E. Foreman, C. A. English, J. T. Buswell, M. G. Hetherington, K. Roberts, and S. Pizzini, ASTM Spec. Tech. Publ. **1125**, 131 (1992).
[6] P. J. Othen, M. L. Jenkins, G. D. W. Smith, and W. J. Phythian, Philos. Mag. Lett. **64**, 383 (1991).
[7] P. J. Othen, M. L. Jenkins, and G. D. W. Smith, Philos. Mag. A **70**, 1 (1994).
[8] R. Monzen, M. L. Jenkins, and A. P. Sutton, Philos. Mag. A **80**, 711 (2000).
[9] P. Auger, P. Pareige, S. Wetzel, and J-C. Van Duysen, J. Nucl. Mater. **280**, 331 (2000), and references therein.
[10] C. S. Becquart and C. Domain, Nucl. Instrum. Methods Phys. Res. B **202**, 44 (2003).
[11] Z. W. Lu, S. H. Wei, and A. Zunger, Phys. Rev. B **41**, 2699 (1990).
[12] C. Domain and C. S. Becqart, Phys. Rev. B **65**, 024103 (2001).
[13] M. S. Daw and M. I. Baskes, Phys. Rev. B **29**, 6443 (1984).
[14] W. J. Phythian, A. J. E. Foreman, C. A. English, J. T. Buswell, M. G. Hetherington, K. Roberts, and S. Pizzini, in Proceedings of the 15th International Symposium on the Effects of Radiation on Materials, Nashville, 1990 ASTM Spec. Tech. Publ. [ASTM Spec. Tech. Publ. **1125**, 131 (1992)].
[15] W. J. Phythian and C. A. English, J. Nucl. Mater. **205**, 162 (1993).
[16] G. J. Ackland, D. J. Bacon, A. F. Calder, and T. Harry, Philos. Mag. A **75**, 713 (1997); See also G. J. Ackland, G. Tichy, V. Vitek, and M. Finnis, *ibid.* **56**, 735 (1987).
[17] Yu. N. Osetsky, A. G. Mikhin, and A. Serra, Philos. Mag. A **72**, 361 (1995).
[18] Yu. N. Osetsky and A. Serra, Philos. Mag. A **73**, 249 (1996).
[19] Yu. N. Osetsky and A. Serra, Philos. Mag. A **75**, 1097 (1997).
[20] G. R. Odette and B. D. Wirth, J. Nucl. Mater. **251**, 157 (1997).
[21] B. D. Wirth and G. R. Odette, in *Microstructural Processes in Infrared Materials*, edited by S. J. Zinkle, G. Leni, R. Ewing, and J. Williams, Mater. Res. Soc. Symp. Proc. No. 540 (Materials Research Society, Pittsburgh, 1999), p. 437.
[22] C. Domain, C. S. Becquart, and J. C. Van Duysen, in Ref. 21, p. 643.
[23] M. Ludwig, D. Farkas, D. Pedraza, and S. Schmauder, Modell. Simul. Mater. Sci. Eng. **6**, 19 (1998).
[24] Y. Le Bouar, Acta Mater. **49**, 2661 (2001).
[25] J. J. Blackstock and G. J. Ackland, Philos. Mag. A **81**, 2127 (2001).
[26] M. W. Finnis and J. E. Sinclair, Philos. Mag. A **50**, 45 (1984).
[27] F. Ercolessi, M. Parrinello, and E. Tosatti, Philos. Mag. A **58**, 213 (1988).
[28] E. O. Arregui, M. Caro, and A. Caro, Phys. Rev. B **66**, 054201 (2002). See also Comput. Mater. Sci. **25**, 297 (2002).
[29] *Molecular-Dynamics Simulation of Statistical-Mechanical Systems*, edited by G. Ciccotti and W. G. Hoover (North-Holland, Amsterdam, 1986).
[30] D. Frenkel and B. Smit, *Understanding Molecular Simulation—From Algorithms to Applications* (Academic Press, London, 1996).
[31] M. Parrinelo and A. Rahman, J. Appl. Phys. **52**, 7182 (1981).
[32] C. Kittel, *Introduction to Solid State Theory*, 6th ed. (Wiley, New York, 1986).
[33] R. Hultgren, R. L. Orr, P. D. Anderson, and K. K. Kelly, *Selected Values of Thermodynamic Properties of Metals and Alloys* (Wiley, New York, 1963).
[34] *Binary Alloy Phase Diagrams*, 2nd ed., edited by T. B. Massalski

(ASM International, Metals Park, OH, 1990).

[35] G. Simonelli, R. Passianot, and E. J. Savino, in *Materials Theory and Modelling*, edited by J. Broughton, P. D. Bristowe, and J. M. Newsam, Mater. Res. Soc. Symp. Proc. No. 291 (Material Research Society, Pittsburgh, 1993), 567.

[36] A. F. Voter (unpublished).

[37] O. Khrushcheva, E. E. Zhurkin, L. Maleaba, C. S. Becqart, C. Domain, and M. Hou, Nucl. Instrum. Methods Phys. Res. B **202**, 68 (2003).